Comparison of simulated powder snow avalanches with photogrammetric measurements

Lisa DREIER,[1] Yves BÜHLER,[1] Christian GINZLER,[2] Perry BARTELT[1]

[1]*WSL Institute for Snow and Avalanche Research SLF, Davos, Switzerland*
[2]*Swiss Federal Institute for Forest, Snow and Landscape Research WSL, Birmensdorf, Switzerland*
Correspondence: Lisa Dreier <lisa.dreier@slf.ch>

ABSTRACT. Photogrammetric measurements of powder-cloud surfaces from large avalanches enable the observation of cloud evolution and dispersion as well as quantification of cloud velocities and powder volumes. Since 2002, a total of six large powder avalanches have been recorded at the test site, Vallée de la Sionne, Switzerland. The high-spatial-resolution photographs, acquired from two different observation angles, allow us to measure the velocity and height of plume-and-cleft structures on the powder-cloud surface. The photogrammetric measurements are supplemented by airborne laser scans of release, entrainment and deposition zones before and after the artificial avalanche release. Even though the precision of the photogrammetric measurements is limited, they are the best data available to test models of powder snow avalanche dynamics. The laser scan data capture initial and boundary conditions while time series of photogrammetric measurements provide insight into mechanisms driving blow-out formation and inertial propagation of the cloud. In this paper we present the experimental measurements and make direct comparisons with model simulations.

KEYWORDS: avalanches, ground-based photogrammetry, powder cloud, powder volume, snow

1. INTRODUCTION

Photogrammetric and videogrammetric methods have been used to measure the spatial and temporal evolution of powder-snow avalanche clouds in three-dimensional (3-D) real-scale terrain (Vallet and others, 2004; Turnbull and McElwaine, 2007). Ice dust blown out of the avalanche core serves as a visible tracer defining the surface of the powder cloud. Photogrammetry is used to construct 3-D powder-cloud manifolds that displace in space and time. It is therefore possible to determine the downward and lateral-spreading velocities of the leading edge of the powder cloud with a temporal resolution equal to the time between two image sets. Plume structures are captured by the measurements and can be used to track the velocities of the cloud behind the leading edge (Bartelt and others, 2013). Coupled with high-spatial-resolution digital elevation models (DEM), the reconstructed surfaces can be used to determine the powder-cloud height and total volume.

The purpose of this paper is to make a direct comparison between measured and simulated powder-cloud velocities and heights in 3-D real-scale terrain. Of particular importance is the spreading velocity of the cloud when it becomes detached from the core and inundates regions beyond the reach of the dense, flowing avalanche core. Accurate modelling of the pressures associated with the spreading of the cloud is often decisive in many practical applications, for both hazard mapping (Bozhinskiy and others, 1998) and back calculations of specific events (Frauenfelder and others, 2014; Honig and others, 2014). Large velocity gradients exist between the leading edge of the avalanche and the avalanche wake and sides (Bartelt and others, 2013). The velocity differences between the leading edge and avalanche wake effectively define the acceleration and drag mechanics operating on the powder cloud. It is therefore possible to distinguish between (1) the acceleration produced by momentum exchanges with the core (leading edge) and (2) the acceleration produced by density differences between the cloud and surrounding air (sides and wake). Most powder-snow avalanche models are based on the second mechanism and therefore require significant snow-cover entrainment to maintain the driving force (Fukushima and Parker, 1990; Ancey, 2004; Rastello and Hopfinger, 2004; Turnbull and McElwaine, 2007; Turnbull and others, 2007; Carroll and others, 2013). Here we apply a two-layer model that accounts for the motion of both the core and the cloud and therefore models both driving mechanisms (Nazarov, 1991; Bozhinskiy and others, 1998; Bartelt and others, 2015a).

An additional feature of the photogrammetric measurements is that they allow monitoring of the intermittent creation of plume structures. The formation of the powder cloud is intimately related to the plume blow-outs, i.e. rapid ejections of ice dust mixed with air that has been entrained and accelerated within the avalanche. The blow-outs effectively define the height of the powder cloud. The deep lobe–cleft structures created by the blow-outs have some permanence and can be used to constrain spatial velocity gradients in the cloud (Bartelt and others, 2013). More importantly, the measured height and volume of the cloud limit the two possible air sources needed to create the cloud's volume: (1) the air taken in at the avalanche front, loaded with ice dust and eventually blown out to create the plumes; and (2) the air entrained directly into the powder cloud, which serves to increase the cloud's volume. Comparing modelled heights and volumes with the photogrammetric measurements helps to constrain the different entrainment mechanisms.

Here we provide a brief overview of the photogrammetric measurements. The governing equations of a two-layer mixed powder-snow avalanche model are then presented (Bartelt and others, 2015a). We then make a one-to-one comparison between the photogrammetric measurements

https://doi.org/10.3189/2016AoG71A532 Published online by Cambridge University Press

Fig. 1. Avalanche path of the mixed flowing-powder avalanche No. 628 at the Vallée de la Sionne avalanche test site. The 20 m high pylon is marked with a black circle.

and model calculations using two well-documented avalanches recorded at the Vallée de la Sionne (Switzerland) avalanche test site (Fig. 1).

2. PHOTOGRAMMETRIC MEASUREMENTS

Measuring avalanche flow characteristics (velocity, height) in 3-D terrain is a difficult task. Measurements are typically performed using devices (e.g. pressure pylon, frequency-modulated continuous-wave (FMCW) radar) positioned along the avalanche track (Sovilla and others, 2005). Fixed-position devices are not only costly (they require power, electronic cabling, etc.) but also must withstand large impact forces. For example, the pressure pylon in Vallée de la Sionne is designed to withstand impact pressures of 800 kPa. However, the major drawback of point-measurement devices is that they capture only a limited part of the avalanche and do not reflect the spatial variation of the avalanche characteristics such as pressure, flow height and velocity. It is therefore impossible to get a sound picture of the avalanche dynamics from point measurements alone.

To overcome the limitations of point devices we make spatially continuous measurements using photogrammetry. Although the spatial resolution and the achieved accuracy of the photogrammetric digital surface models (DSM) is limited, they enable spatially continuous observation of the powder cloud velocity and volume and also track features on the cloud surface. The Vallée de la Sionne test site is optimal for photogrammetric measurements because the cameras can be installed on the safe counterslope, enabling a good view of nearly the entire avalanche track.

At the Vallée de la Sionne avalanche test site, photogrammetric measurements have been carried out since 2002 to visualize the formation and development of powder-cloud avalanches (Vallet and others, 2004). In winter 2003/04 three Sony DCR-TRV-900 video cameras providing 768×756 pixels were installed on the counterslope facing the avalanche path (Wicki, 2004; Sovilla and others, 2005; Wicki and Laranjeiro, 2007). The two cameras that provided the data for the photogrammetric analysis recorded at 25 frames s^{-1} and defined a baseline 250 m long. The calibrated focal length was 4.5 mm and the accuracy of parallax measurements was ~2.5 μm. With this configuration a theoretical accuracy should be reached of ±10 m in the upper part and ±5 m in the lower part of the avalanche path (Vallet and others, 2004; Sovilla and others, 2005). The distance between the cameras and the powder cloud ranged between 2600 m (release zone) and 600 m (deposition zone). The measurement accuracy increases the shorter the distance between the cameras and the object. For the photogrammetric analysis, simultaneously recorded images were selected to reconstruct the powder-cloud surface. The quality of powder-snow height measurements is strongly dependent on the images' contrast. No measurements can be performed in low-contrast areas.

Accuracy measurements of the absolute orientation of the model in the vertical direction showed that powder-cloud height measurements have an estimated error of ±10 m. Absolute powder cloud heights therefore need to be treated with caution. Analysis of the relative agreement between successive images instead allows us to derive a reliable picture of the formation and development of the powder cloud (Sovilla and others, 2005). The cameras that recorded the data for the photogrammetric measurements in winter 2003/04 are now outdated. Today, state-of-the-art cameras offering 24×10^6 pixels and advanced analysis software would provide less labour-intensive data analysis and more precise photogrammetric measurements.

For every stereo-image measurement the avalanche front lines and a DSM of the powder-cloud surface were digitized manually. The grid resolution of the DSM is 10 m. It is possible to calculate front velocity by dividing the travelled distance of the avalanche front by the interval between successive time frames. Generating a height map of the powder cloud (Fig. 2) by subtracting the digital terrain model from the DSM enables us to determine powder-cloud volume. When particles settle at the tail of the avalanche (near the release zone) the cloud often becomes diluted to the point where it is no longer visible, making it impossible to determine powder-cloud height (Fig. 4a) or to calculate its volume (Bartelt and others, 2013). However, the average powder-cloud height can be determined for specific regions in the cloud with strong contrast. Development and formation of the powder cloud can be demonstrated by showing the evolution of the powder-cloud height at different points along the avalanche path (Fig. 6) or by visualizing powder-cloud height as a profile along the avalanche path at different time steps (Fig. 7).

As well as the photogrammetric measurement installation, the Vallée de la Sionne avalanche test site is equipped with pressure sensors at the pylon measuring the avalanche core pressure at different heights, and two upward-looking FMCW radars. From the data recorded by the FMCW radars

https://doi.org/10.3189/2016AoG71A532 Published online by Cambridge University Press

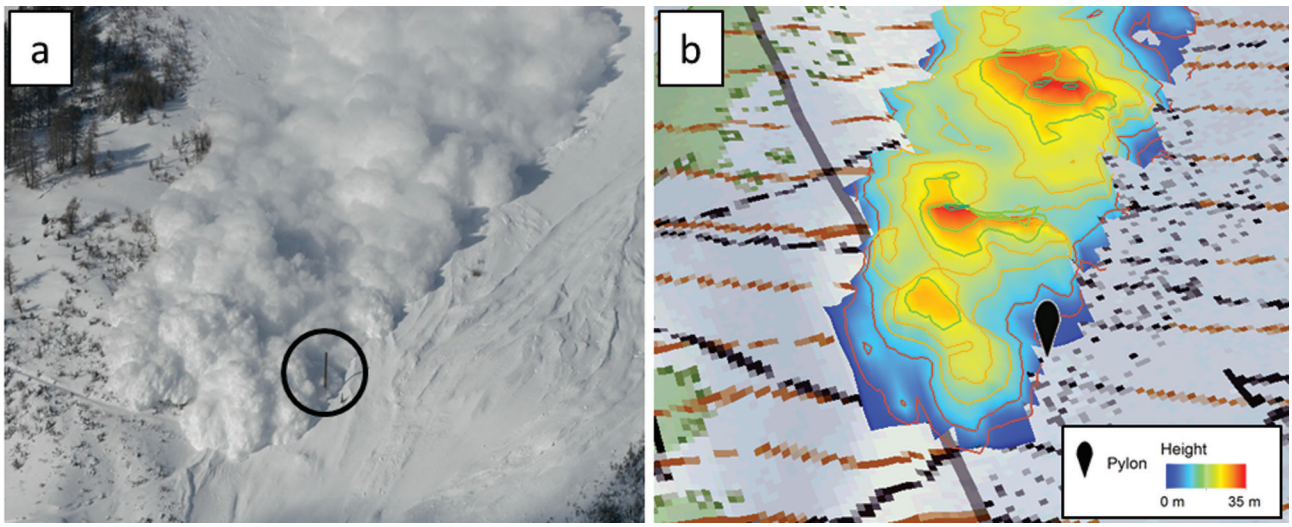

Fig. 2. (a) Avalanche No. 628 on 19 January 2004 at the Vallée de la Sionne reaching the 20 m pylon indicated by the black circle. (b) Surface of the powder cloud obtained with photogrammetric analysis. Black marker indicates position of pylon.

we can derive the avalanche core height over time at the radar location.

3. TWO-LAYER MODEL EQUATIONS

To model powder snow avalanches, we apply the two-layer model of Bartelt and others (2015a). Two-layer models consist of an avalanche core Φ and a powder cloud Π. The state variables for the core are

$$\mathbf{U}_\Phi = (M_\Phi, M_\Phi u_\Phi, M_\Phi v_\Phi, Rh_\Phi, h_\Phi, M_\Phi w_\Phi, N_K)^T \quad (1)$$

and for the cloud

$$\mathbf{U}_\Pi = (M_\Pi, M_\Pi u_\Pi, M_\Pi v_\Pi, h_\Pi)^T. \quad (2)$$

The flow velocity of the core is given by the slope-parallel two-dimensional vector $\mathbf{u}_\Phi = (u_\Phi, v_\Phi)^T$; similarly for the powder cloud, $\mathbf{u}_\Pi = (u_\Pi, v_\Pi)^T$. The velocity of the avalanche core in the slope-perpendicular direction is w_Φ. Slope perpendicular velocities are generated when the free mechanical energy R (J m^{-3}) of the avalanche is deflected at the basal boundary, creating the dispersive pressure N_K (Bartelt and others, 2015a; Buser and Bartelt, 2015). Core and cloud masses per unit area are denoted M_Φ and M_Π, respectively. Flow heights measured from the basal boundary for the core and the cloud are designated h_Φ and h_Π.

The motion of the mixed avalanche is found by solving the differential equations

$$\frac{\partial \mathbf{U}_\Phi}{\partial t} + \frac{\partial \mathbf{\Phi}_x}{\partial x} + \frac{\partial \mathbf{\Phi}_y}{\partial y} = \mathbf{G}_\Phi \quad (3)$$

$$\frac{\partial \mathbf{U}_\Pi}{\partial t} + \frac{\partial \mathbf{\Pi}_x}{\partial x} + \frac{\partial \mathbf{\Pi}_y}{\partial y} = \mathbf{G}_\Pi. \quad (4)$$

The flux components for the core ($\mathbf{\Phi}_x$, $\mathbf{\Phi}_y$) are

$$\mathbf{\Phi}_x = \begin{pmatrix} M_\Phi u_\Phi \\ M_\Phi u_\Phi^2 + \frac{1}{2} M_\Phi g' h_\Phi \\ M_\Phi u_\Phi v_\Phi \\ Rh_\Phi u_\Phi \\ h_\Phi u_\Phi \\ M_\Phi w_\Phi u_\Phi \\ N_K u_\Phi \end{pmatrix}, \quad \mathbf{\Phi}_y = \begin{pmatrix} M_\Phi v_\Phi \\ M_\Phi u_\Phi v_\Phi \\ M_\Phi v_\Phi^2 + \frac{1}{2} M_\Phi g' h_\Phi \\ Rh_\Phi v_\Phi \\ h_\Phi v_\Phi \\ M_\Phi w_\Phi v_\Phi \\ N_K v_\Phi \end{pmatrix} \quad (5)$$

and the flux components of the cloud ($\mathbf{\Pi}_x$, $\mathbf{\Pi}_y$) are

$$\mathbf{\Pi}_x = \begin{pmatrix} M_\Pi u_\Pi \\ M_\Pi u_\Pi^2 + \frac{1}{2} M_\Pi g_z h_\Pi \\ M_\Pi u_\Pi v_\Pi \\ h_\Pi u_\Pi \end{pmatrix}, \quad \mathbf{\Pi}_y = \begin{pmatrix} M_\Pi v_\Pi \\ M_\Pi u_\Pi v_\Pi \\ M_\Pi v_\Pi^2 + \frac{1}{2} M_\Pi g_z h_\Pi \\ h_\Pi v_\Pi \end{pmatrix}. \quad (6)$$

The core of the avalanche is driven by the gravitational acceleration in the tangential directions $\mathbf{G} = (G_x, G_y) = (M_\Phi g_x, M_\Phi g_y)$. Gravitational acceleration is decomposed into three gravitational components, $\mathbf{g} = (g_x, g_y, g_z)$. This gives rise to the two driving terms $\mathbf{G}_\Phi$ and $\mathbf{G}_\Pi$ of the two-layer model system:

$$\mathbf{G}_\Phi = \begin{pmatrix} \dot{M}_{\Sigma\to\Phi} - \dot{M}_{\Phi\to\Pi} \\ G_x - S_{\Phi x} - \dot{M}_{\Phi\to\Pi} u_\Phi \\ G_y - S_{\Phi y} - \dot{M}_{\Phi\to\Pi} v_\Phi \\ \alpha(\mathbf{S}_\Phi \cdot \mathbf{u}_\Phi) - \beta R_K \\ w_\Phi \\ N_K \\ 2\gamma \dot{P} - 2N w_\Phi / h_\Phi \end{pmatrix} \quad (7)$$

and

$$\mathbf{G}_\Pi = \begin{pmatrix} \dot{M}_{\Phi\to\Pi} + \dot{M}_{\Lambda\to\Pi} \\ \dot{M}_{\Phi\to\Pi} u_\Phi - S_{\Pi x} \\ \dot{M}_{\Phi\to\Pi} v_\Phi - S_{\Pi y} \\ \dot{V}_{\Phi\to\Pi} + \dot{V}_{\Lambda\to\Pi} \end{pmatrix}. \quad (8)$$

The driving terms $\mathbf{G}_\Phi$ and $\mathbf{G}_\Pi$ contain the mass and momentum exchanges with the surrounding air (subscript Λ) and snow cover (subscript Σ). The mass exchanges in the mixed flowing avalanche system are (1) snow entrainment into the avalanche core $\dot{M}_{\Sigma\to\Phi}$, (2) volume and mass blow-out of ice dust from the core $\dot{V}_{\Phi\to\Pi}$ and $\dot{M}_{\Phi\to\Pi}$ and (3) direct air entrainment into the powder cloud $\dot{V}_{\Lambda\to\Pi}$ (volume) and $\dot{M}_{\Lambda\to\Pi}$ (mass). The model of snow-cover entrainment is described by Christen and others (2010). The normal pressure increases during the expansion of the avalanche core, which facilitates the intake of air into the avalanche. This air is mixed with ice dust and is blown out when the core volume contracts (Buser and Bartelt, 2015). The speed of the blow-out is thus related to the speed of the core

https://doi.org/10.3189/2016AoG71A532 Published online by Cambridge University Press

contraction. The powder cloud height h_Π is measured from the ground and includes the volume of the flowing avalanche core. The fluidization parameters α, β and γ define the volume of air blown out of the core, $\dot{V}_{\Phi\to\Pi}$. This air is mixed with ambient air above the core. The intake of ambient air is parameterized by the condition

$$\dot{M}_{\Lambda\to\Pi} = \kappa_\Pi(\rho_\Pi - \rho_a), \tag{9}$$

where κ_Π is the air entrainment coefficient with dimension length and ρ_a is the density of air (without ice dust). In the simulations we use $\kappa_\Pi = 6$ m. This value provides good agreement with the photogrammetric measurements.

Central to the model equations is the inclusion of the free mechanical energy R of the avalanche core, which is the sum of the energy of the random granule motions R_K (Bartelt and others, 2006) and configurational (density) changes R_V (Buser and Bartelt, 2015),

$$R = R_K + R_V. \tag{10}$$

R_V is the free mechanical energy associated with the different granule locations and is therefore related to the core flow density. Both R_K and R_V are produced by shearing in the avalanche core. The production rates of free mechanical energy are $\dot{P}_K$ and $\dot{P}_V$, respectively. The production and decay rates of the free mechanical energy are governed by the interaction with the basal boundary as the kinetic energy of the random particle movements is transformed into potential energy at the boundary. This transformation requires partitioning. The fraction of mechanical energy $\dot{P}_V$ with respect to the total $\dot{P}$ is the dimensionless quantity γ:

$$\dot{P}_V = \gamma\dot{P} \qquad \dot{P}_K = (1-\gamma)\dot{P}. \tag{11}$$

The dispersive pressure N_K and vertical velocity w_Φ arise from the changes in configurational energy R_V (Buser and Bartelt, 2011, 2015).

The total free mechanical energy is produced from the rate of working of the total shear work $\alpha(\mathbf{S}_\Phi \cdot \mathbf{u}_\Phi)$, the model parameter α describing the production rate $0 \le \alpha \le 0.1$ (Buser and Bartelt, 2009). The kinetic part of the fluctuation energy R_K decays according to the parameter β because of irreversible collisional/frictional interactions in the avalanche core. Wet snow avalanches with moist granules have higher decay rates than dry snow granules. For shearing in the core $\mathbf{S}_\Phi = (S_{\Phi x}, S_{\Phi y})$ we use a Voellmy-type ansatz:

$$\mathbf{S}_\Phi = \frac{\mathbf{u}_\Phi}{\|\mathbf{u}_\Phi\|}\left[\mu(R_V, N_0)N + \rho_0 g\frac{\|\mathbf{u}_\Phi\|^2}{\xi(R_V)}\right]. \tag{12}$$

Coulomb friction in the core (parameter μ) is adjusted to account for snow cohesion N_0 (Bartelt and others, 2015b). The normal pressure N includes the weight of the avalanche itself, centripetal and dispersive pressures. The corresponding acceleration is g'. Both the Coulomb friction $\mu(R_V, N_0)$ and turbulent friction $\xi(R_V)$ depend on the configurational energy content of the core R_V. The static friction values μ_0 and ξ_0 are exponentially reduced to account for lower flow densities associated with higher configurational energy R_V (Christen and others, 2010). The reduction is controlled by the activation energy R_0 (Bartelt and others, 2012). Therefore, μ and ξ correspond to the friction when the avalanche is flowing with density ρ, while μ_0 and ξ_0 correspond to the friction when the avalanche core is at rest with density ρ_0. Drag on the powder cloud $\mathbf{S}_\Pi = (S_{\Pi x}, S_{\Pi y})$ is given by a velocity-squared type law:

$$\mathbf{S}_\Pi = \frac{\mathbf{u}_\Pi}{\|\mathbf{u}_\Pi\|}\left[\rho_\Pi g\frac{\|\mathbf{u}_\Pi\|^2}{\xi_\Pi}\right]. \tag{13}$$

Cloud drag is primarily governed by turbulent air entrainment $\dot{M}_{\Lambda\to\Pi}$.

4. VALLÉE DE LA SIONNE AVALANCHE NO. 628

On 19 January 2004 a mixed flowing-powder avalanche (No. 628) was artificially released at the Vallée de la Sionne avalanche test site (Fig. 1). We selected avalanche No. 628 because the entire event was very well documented. The avalanche released in steep terrain near the upper ridge of the Crêta Besse I release zone at 2600 m. Photogrammetric images were created from the start of the avalanche ($t = 0$) until it passed the measurement mast ($t = 55$ s). The digital surface of the powder cloud was reconstructed at 5 s intervals starting at $t = 20$ s. Beginning at $t = 50$ s, when the avalanche flowed past the measurement pylon (Fig. 2), the reconstructions were made at 1 s intervals. The avalanche travelled the entire length of the avalanche path, reaching the valley bottom (1400 m) and running up the counter-slope. The measurement pylon at approximately 1650 m was hit marginally.

Helicopter-based laser scanning was used to delineate the avalanche starting zone as well as to determine snow-cover entrainment/deposition depths. These measurements revealed an average release depth $h = 0.80$–0.90 m and a release volume $V_0 = 20\,000$ m^3. Snow measurements in the release zone after the event indicated that the average density of the starting mass was $\rho = 250$ kg m^{-3}. The density $\rho_0 = 450$ kg m^{-3} corresponds to the typical density of hardened snow blocks and granules found in snow avalanches. Moreover, the fracture slab starts as a homogeneous layer with low density but granularizes into hardened snowballs. A mean entrainment depth of 0.23 m was estimated from the laser-scanning measurements. The deposited mass was approximately 14 000 t (Sovilla and others, 2005). Model calculations were performed using these values. We apply the same model parameters for the flowing avalanche core as those adopted by Bartelt and others (2006, 2012, 2015a), Christen and others (2010) and Buser and Bartelt (2015). These are $\mu_0 = 0.55$, $\xi_0 = 1800$ m s^{-2}, $N_0 = 50$ Pa, $\alpha = 0.08$, $\beta = 0.85$ and $R_0 = 2.0$.

4.1. Avalanche-front velocity

A comparison between the measured and simulated locations of the avalanche leading edge is provided in Table 1. The avalanche gains speed when running through the gully situated in the middle of the transit zone. Front velocities increase to nearly 60 m s^{-1} at the gully exit and decrease in the open terrain where the pylon is situated. These results are in agreement with other findings (Vallet and others, 2004), which report a maximum front velocity of 55 m s^{-1} in the gully for similar avalanche release conditions. The simulated avalanche needed 6.5 s, i.e. 1.5 s longer, to advance from the position of the leading edge as measured at $t = 20$ s to that measured at $t = 25$ s. That is, the calculated front velocity is lower than measured. Compared to the measurements, from $t = 25$ s to $t = 51$ s the simulated avalanche-arrival times are all shifted by +1.5 s. Thus, after an initial delay, the measured and calculated leading-edge

https://doi.org/10.3189/2016AoG71A532 Published online by Cambridge University Press

velocities are in good agreement. During this time, the avalanche travels over 1 km. The simulated avalanche loses another 0.5 s between $t = 51$ s and $t = 55$ s. The largest difference between the measured and calculated avalanche velocity occurs between $t = 51$ s and $t = 52$ s. Because this mismatch lasts only for 1 s, the difference in measured and calculated avalanche position is small. Estimated uncertainties of front velocities amount to a maximum of 8 m s^{-1} due to possible errors in the location of the photogrammetric measurements of up to 4 m (Wicki, 2004). Additional inaccuracy might be added by the selection of points for measuring the travelled distance. Although the agreement between calculated and measured front velocity is good, we emphasize that front velocity alone is not adequate for evaluating powder-snow avalanche models. Of considerable importance is the formation of the avalanche wake (no velocity) as well as the lateral spreading of the powder cloud. These are considered in the next subsections.

4.2. Powder-cloud volume

The measured powder-cloud volume increases linearly from 0.0 to 0.5×10^6 m^3 (Table 1). Measured volume depends on the surface area of the reconstruction. For example, powder-cloud volume calculations of similar avalanches released in winter 2002/03 and 2004/05 increased exponentially up to 8×10^6 m^3 (Vallet and others, 2004; Turnbull and McElwaine, 2007; Bartelt and others, 2013). The latter measurements included much of the avalanche wake and therefore the reconstructed volumes were larger. Because of the low contrast at the tail of the No. 628 avalanche, the surface reconstructions could not be performed and therefore the volume of the wake was not included in the total avalanche volume. To overcome this difficulty, we divided the powder cloud volume by the reconstructed surface area (of good contrast) to obtain the average powder cloud height. The average height of the powder cloud derived from the simulation results matches the measurements (Fig. 3). This is an indication that the growth of the powder cloud in the wake is small and does not contribute to the volume growth. The powder cloud is created primarily at the avalanche front. This supports the implicit assumption of the two-layer avalanche model.

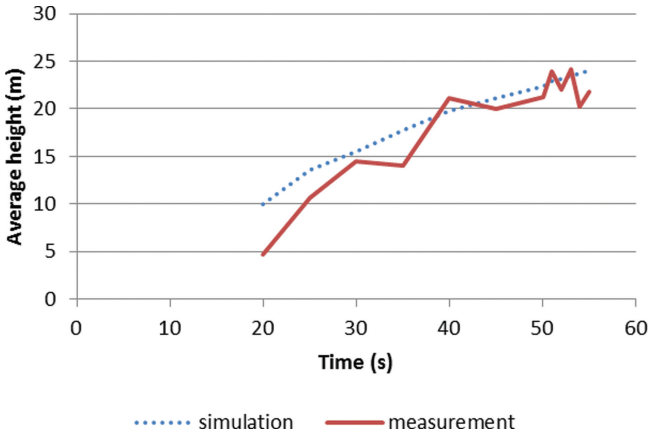

Fig. 3. Average height of powder cloud over time of avalanche No. 628. The average height of both the measurements and simulations was found by dividing the reconstructed volume by the surface area. Surface regions with low contrast, especially at the avalanche wake, are difficult to include in the volume measurements.

4.3. Cloud width and surface structure

The comparison between the measured and calculated average powder height is useful for engineering applications but does not provide detailed information on the location of the plume formation or the spatial distribution of powder-cloud heights. A comparison between the reconstructed and simulated powder-cloud heights at $t = 54$ s over the entire avalanche length is shown in Figure 4. This depiction reveals the rough, heterogeneous surface of the measurements in comparison to the smooth powder cloud surface of the model calculations. The outer edge of the measurements is serrated, highlighting the intermittent formation process, whereas the outer edge of the calculated avalanche is smooth, reflecting the averaging process of the numerical approximation. The reconstructed surfaces exhibit a lobe-and-cleft structure; the model calculations do not simulate the surface depressions between plumes. However, the surface area covered by the calculated powder cloud is remarkably similar to the surface area of the measurements (Fig. 4b). Note that the model captures the location and shape of the avalanche front. Of considerable importance is

Table 1. Measurement time and simulation time steps with derived front velocity. The simulation time is the time when the simulated avalanche reaches the measured leading edge of the avalanche. The front velocity is calculated by dividing the travelled distance by the time the avalanche needs to cover the distance. Simulated front velocities equal measurements or are underestimated

Measurement time	Simulation time	Distance travelled	Measured velocity	Simulated velocity	Velocity difference	Measured volume
s	s	m	m s^{-1}	m s^{-1}	m s^{-1}	m^3
20	20.0	–	–	–	–	3078
25	26.5	170	34.0	26.2	7.8	37 762
30	31.0	171	34.2	38.0	–3.8	82 874
35	36.5	169	33.8	30.7	3.1	84 374
40	41.5	179	35.8	35.8	0.0	298 329
45	46.5	221	44.2	44.2	0.0	276 831
50	51.5	214	42.8	42.8	0.0	368 999
51	52.5	58	58.0	58.0	0.0	440 360
52	54.0	35	35.0	23.3	11.7	421 180
53	55.0	33	33.0	33.0	0.0	477 419
54	56.0	36	36.0	36.0	0.0	425 769
55	57.0	36	36.0	36.0	0.0	472 502

https://doi.org/10.3189/2016AoG71A532 Published online by Cambridge University Press

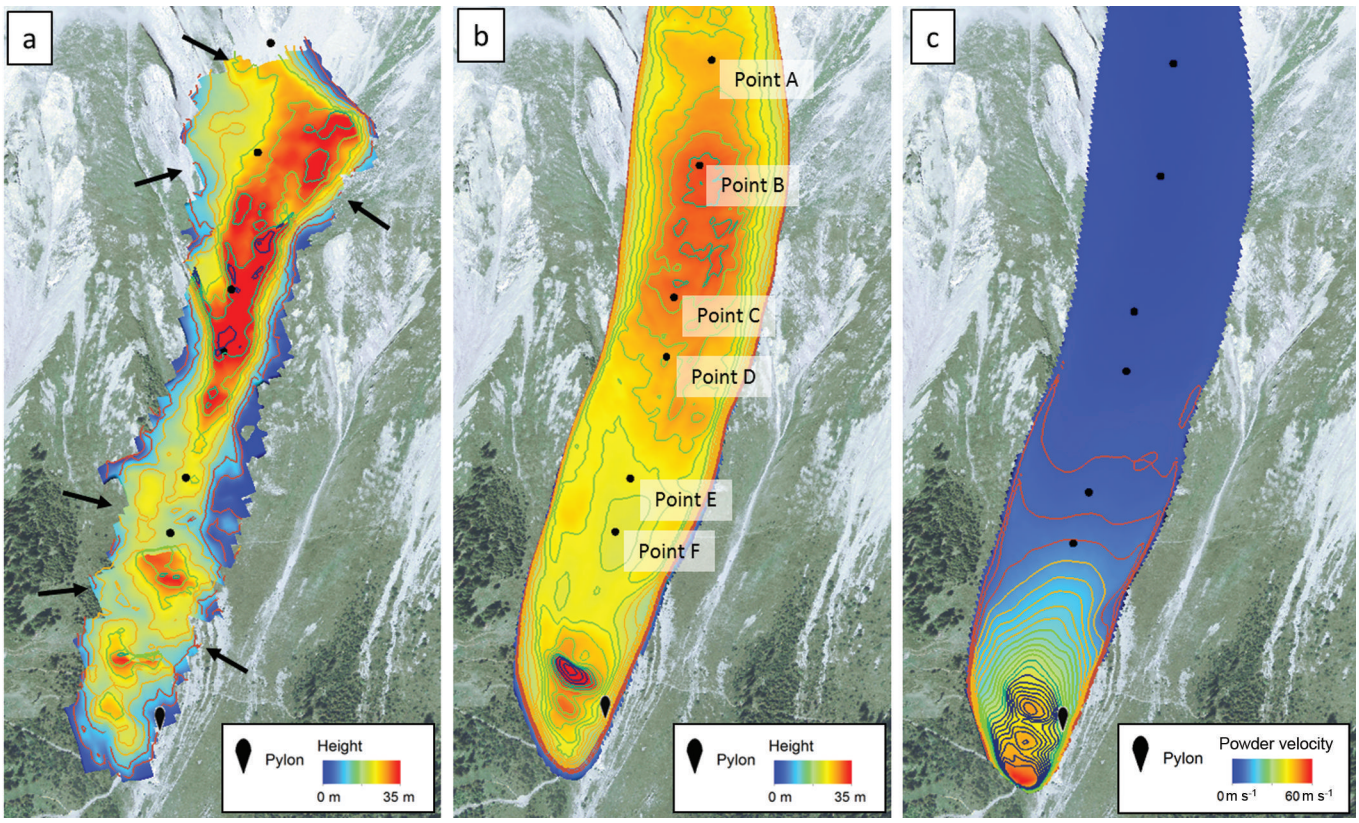

Fig. 4. Powder cloud of avalanche No. 628 at $t = 54$ s. (a) Photogrammetric reconstruction and (b) calculated powder-cloud height; (c) calculated powder-cloud velocity. The model calculations overestimate the powder-cloud height and do not capture cleft depressions between plumes. Black arrows mark missing parts of the measured cloud surface. At the tail of the avalanche the missing surfaces might be due to particle settlement diluting the cloud to a point where it is no longer visible, or might result from poor image contrast. High plumes and/or poor visibility (e.g. fog) can also mask the surface, preventing an accurate reconstruction. Black dots mark points along the avalanche path used to compare the calculated results with the measurements (see Fig. 6). The calculations model a fast-moving leading edge and a stationary wake.

the calculated velocity distribution. The wake of the avalanche is stationary in comparison to the front, which is moving at the speed of the avalanche core (Fig. 4c). The wake does not spread laterally, providing good agreement between the measured and simulated avalanche flow width. A primary difference between the measured and calculated surface is the height of the cloud at the lateral boundary. The edge of the simulated cloud is steeper, indicating that the air entrainment is overestimated.

Maximum cloud heights of nearly 90 m were measured at time step 53 s just above point C (Fig. 4b). The maximum measured cloud height is much higher than the simulated maximum of nearly 50 m. The maximum cloud heights occurred when the avalanche ran through the gully and the flow was constricted. The model assumes that air blow-out is defined by the slope-perpendicular collapse of the avalanche core. The poor agreement between the measured and calculated maximum powde-cloud heights in this region is perhaps an indication that slope-parallel velocity gradients that lead to a core densification should also contribute to the blow-out process and the formation of the powder cloud. The calculated mean density of the powder cloud at the wake is only $\rho_{\Pi} = 1.5$ kg m^{-3}, indicating a dilute and therefore transparent cloud.

A close-up view of the powder-cloud front in Figure 5 compares the measured powder-cloud heights with the model calculations. The calculations appear to model the plumes labelled A and B. The plume at location C, however, disappears. The disappearance of plume C is due to excess air entrainment at the lateral edges of the cloud, which increases the powder height too much, creating a depression in the cloud interior.

4.4. Powder-cloud height

The evolution of the powder cloud at selected points in the terrain is shown in Figure 6. The points are located along the avalanche path (Fig. 4b). The topmost point, A, is located 300 vertical metres below the release area. The lowermost point, F, is located approximately 100 vertical metres above the pylon. Powder-cloud heights are much greater in the gully (points B–D) than on the slope above the gully (point A) or in the open terrain below the gully (points E and F). This is an indication that flow constriction, and therefore core densification, contributes to the formation of the powder cloud. The calculated powder-cloud heights match the measured heights well. However, the exact form of the blow-out is often not reproduced. For example, in Figure 6 at point D, the calculated plume height is over-predicted, whereas in Figure 6 at point E the plume height and depression appear to be well modelled. Only at the start of the gully (point B) are powder-cloud heights underestimated by the model.

Two-dimensional longitudinal sections of the powder-cloud height were created in order to examine the spatial distribution of powder-cloud heights from the front of the avalanche to the wake (Fig. 7). The profile began from the

https://doi.org/10.3189/2016AoG71A532 Published online by Cambridge University Press

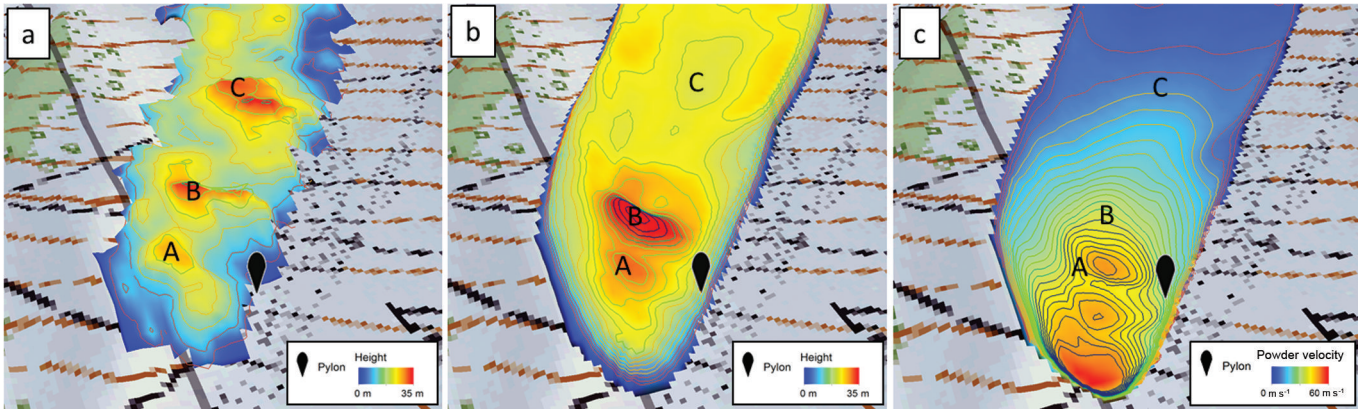

Fig. 5. Close-up of the avalanche front at $t = 54$ s. (a) Photogrammetric reconstruction and (b) calculated powder-cloud height; (c) calculated powder-cloud velocity. Plumes at locations A and B are reproduced, whereas the plume at location C disappears because the air entrainment at the lateral edges of the cloud is too large. The velocity of the powder cloud decreases rapidly behind the front.

release area and ended 50 m below the pylon, located at ~1650 m. Profiles were created for the measurement times $t = 20$ s, 30 s, 40 s, 50 s, 52 s and 54 s. The plumes reach maximum heights of more than 40 m when the avalanche reaches the beginning of the gully at a distance of approximately 600 m from the release area (see, e.g., measurement at 40 s in Fig. 7). At the upper end of the gully the avalanche travels at 44 m s^{-1} (see 45 s in Table 1). In the open terrain below the gully, about 1000 m from the release area, the plume heights decrease. The measurements and simulation results show continuous but intermittent formation of plumes at the avalanche front. In the avalanche wake the plumes are essentially stationary (Figs 8 and 4c). These findings are in line with the analysis of the powder-cloud volume in Section 4.2. The model appears to underestimate the plume blow-outs and the depth of the plume depressions (see also Section 4.3), providing powder-cloud heights that are on average in good agreement with the photogrammetric measurements (Fig. 3).

4.5. Additional measurements

Other measurements recorded during the avalanche event can be used to verify the simulation results. The simulated pressure of the avalanche core at the pylon ($p = 130$ kPa) corresponds to the measured pressure ($p = 150$ kPa). The pressure sensor was located at a height of 2.5 m. The calculated value corresponds to a uniform avalanche velocity in the core. The signal lasts 35 s in the measurements and 25 s in the simulation. The avalanche core height derived from the FMCW radar signal is nearly $h_\Phi = 7$ m at the

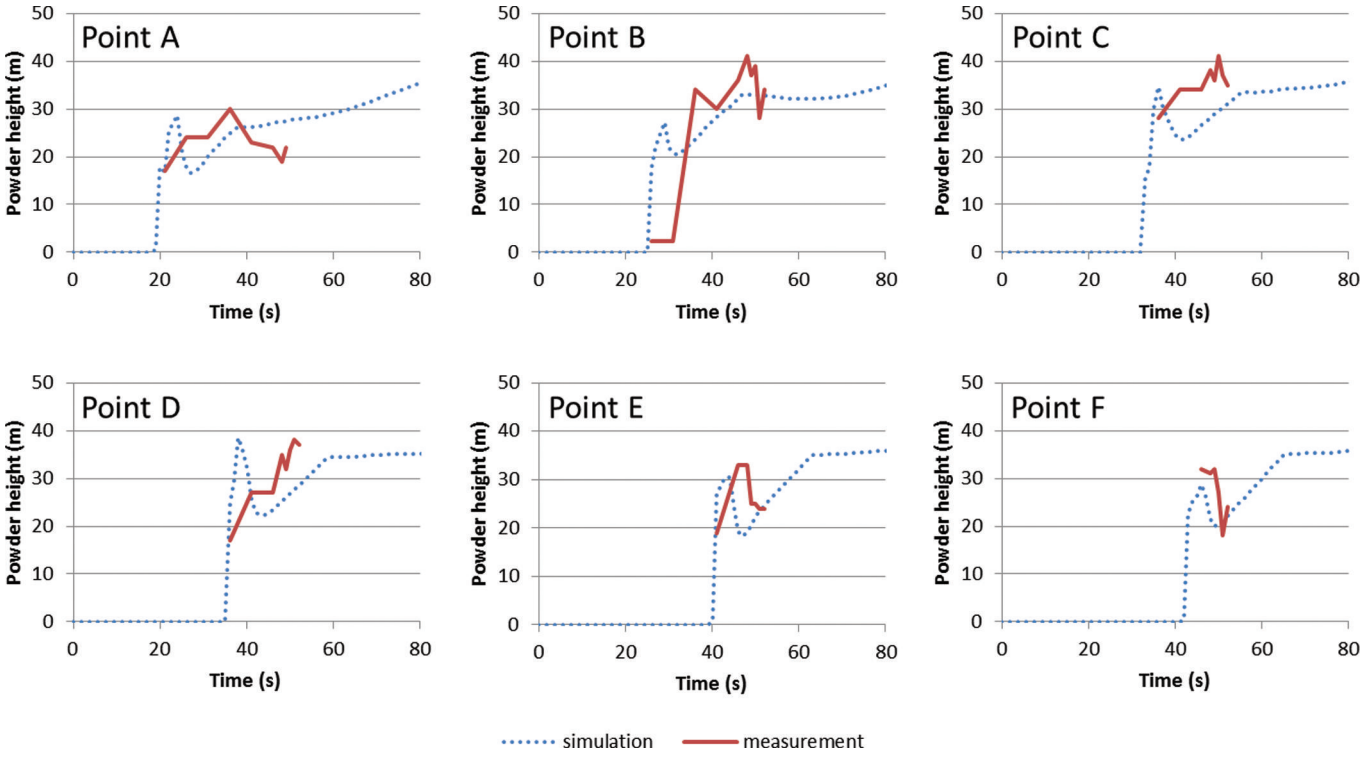

Fig. 6. Height of powder cloud over time at points along the avalanche No. 628 path. Figures are ordered from the topmost point, A, 300 vertical metres below the release area, to the lowermost point, F, 100 vertical metres above the pylon. The location of the points is marked in Figure 4b.

https://doi.org/10.3189/2016AoG71A532 Published online by Cambridge University Press

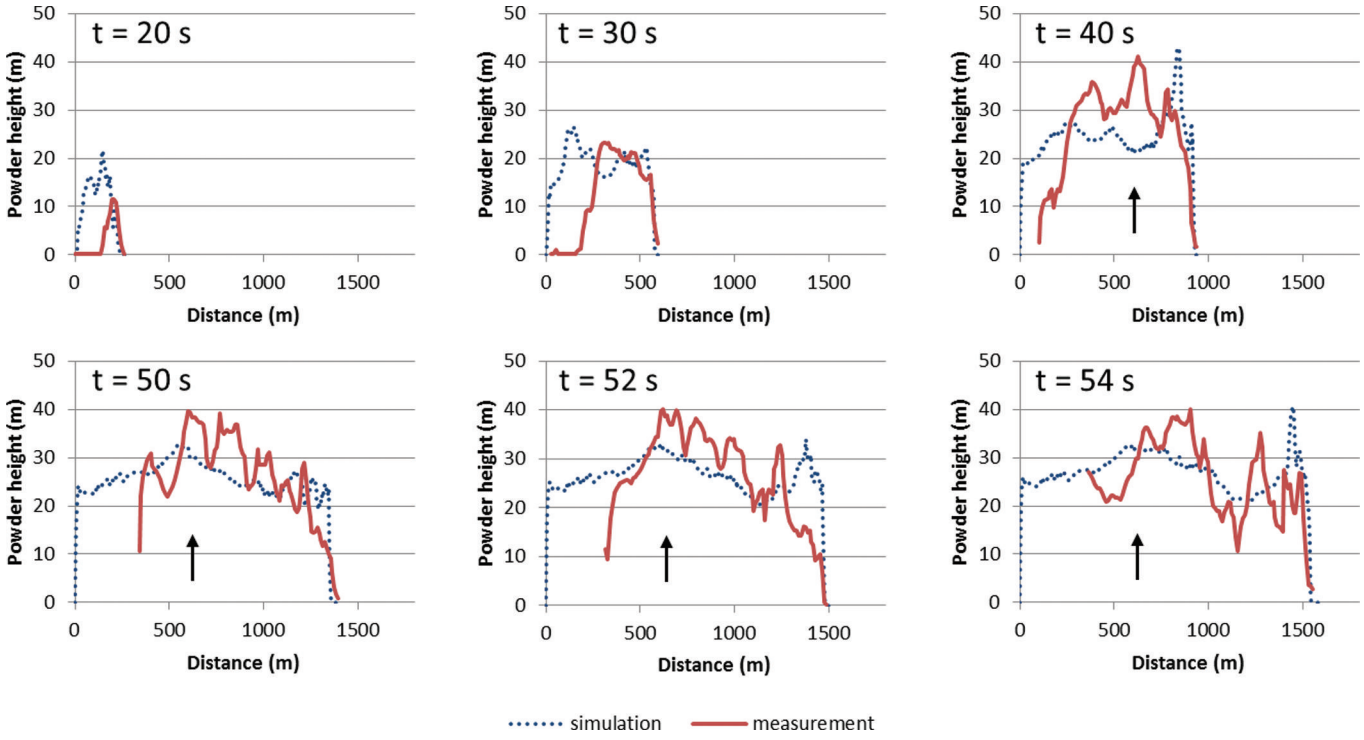

Fig. 7. Powder-cloud heights along a specified profile from the release area to 50 vertical metres below the pylon throughout the length of the path of avalanche No. 628 at different times after artificial release. A black arrow marks the beginning of the gully.

avalanche front, decreasing towards the avalanche tail. A second peak with a height of $h_\Phi = 2$–3 m is also visible in the radar signal. The signal duration of the avalanche over the radar is 10 s. Both the height and duration of the calculated avalanche core at the location of the FMCW radars correspond well with the measurements. The core heights of the avalanche are slightly overestimated at the avalanche front, $h_\Phi = 7.5$ m, and underestimated towards the tail, the second peak amounting to only $h_\Phi = 1$–2 m.

5. VALLÉE DE LA SIONNE AVALANCHE NO. 816

To further test the model, an additional mixed flowing/powder-snow avalanche was investigated. Vallée de la Sionne avalanche No. 816 was artificially triggered on 6 March 2006. Whereas avalanche No. 628 descended as a single-lobe avalanche, avalanche No. 816 had three distinct flow arms, each accompanied by a powder cloud (Fig. 9, at $t = 50$ s). Atmospheric clouds obscured the orographic right side of the movement and therefore the photogrammetric reconstruction was performed only for the orographic left side. This flow arm followed the main Vallée de la Sionne channel. The red line in Figure 9 indicates the cut-off line defining where the photogrammetric reconstruction was performed. It was therefore not possible to determine the total powder-cloud volume. In winter 2005/06 two CANON EOS 20D cameras with 3504×2336 px replaced the older cameras used for avalanche No. 628, increasing the accuracy of the powder-cloud surface reconstruction to 2–3 m (Wicki, 2005).

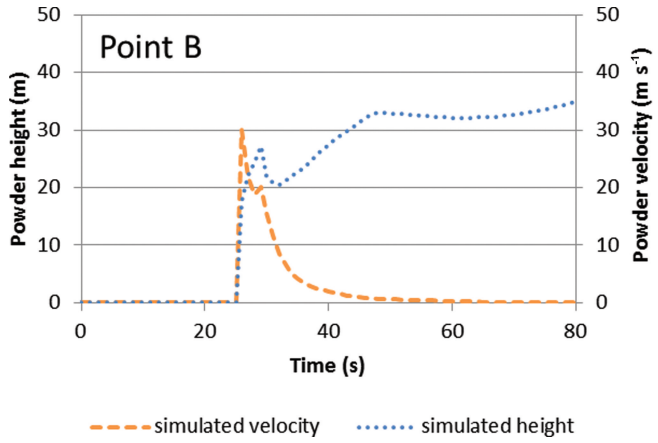

Fig. 8. Calculated height and velocity of the powder cloud of avalanche No. 628 over time at point B (marked in Fig. 4b). The simulation results show a fast-moving leading edge and a stationary wake.

Measurements obtained with helicopter-based laser scanning revealed an average release depth of $h = 1.5$ m and a release volume of $V_0 = 30\,000$ m^3. Steinkogler and others (2014) modelled the snow cover using meteorological input from the Vallée de la Sionne weather station and predicted the average density of the starting mass to be $\rho = 180$ kg m^{-3}. These values were used in the simulation to define the initial conditions. The laser scanning measurement also revealed a mean entrainment depth of 0.40 m. Again using snow-cover model simulations, the temperature of the entrained snow was calculated to be $T_\Sigma = -5$°C at the time of the event. We applied the following parameter values in the model calculations: $\mu_0 = 0.55$, $\xi_0 = 2000$ m s^{-2}, $N_0 = 50$ Pa, $\rho_0 = 450$ kg m^{-3} and $R_0 = 2.0$, similar to avalanche No. 628.

In avalanche No. 628 we modelled snow entrainment as a perfectly plastic collision between the avalanche and the snow cover. With avalanche No. 816 we assumed some elasticity during the snow-cover entrainment process,

https://doi.org/10.3189/2016AoG71A532 Published online by Cambridge University Press

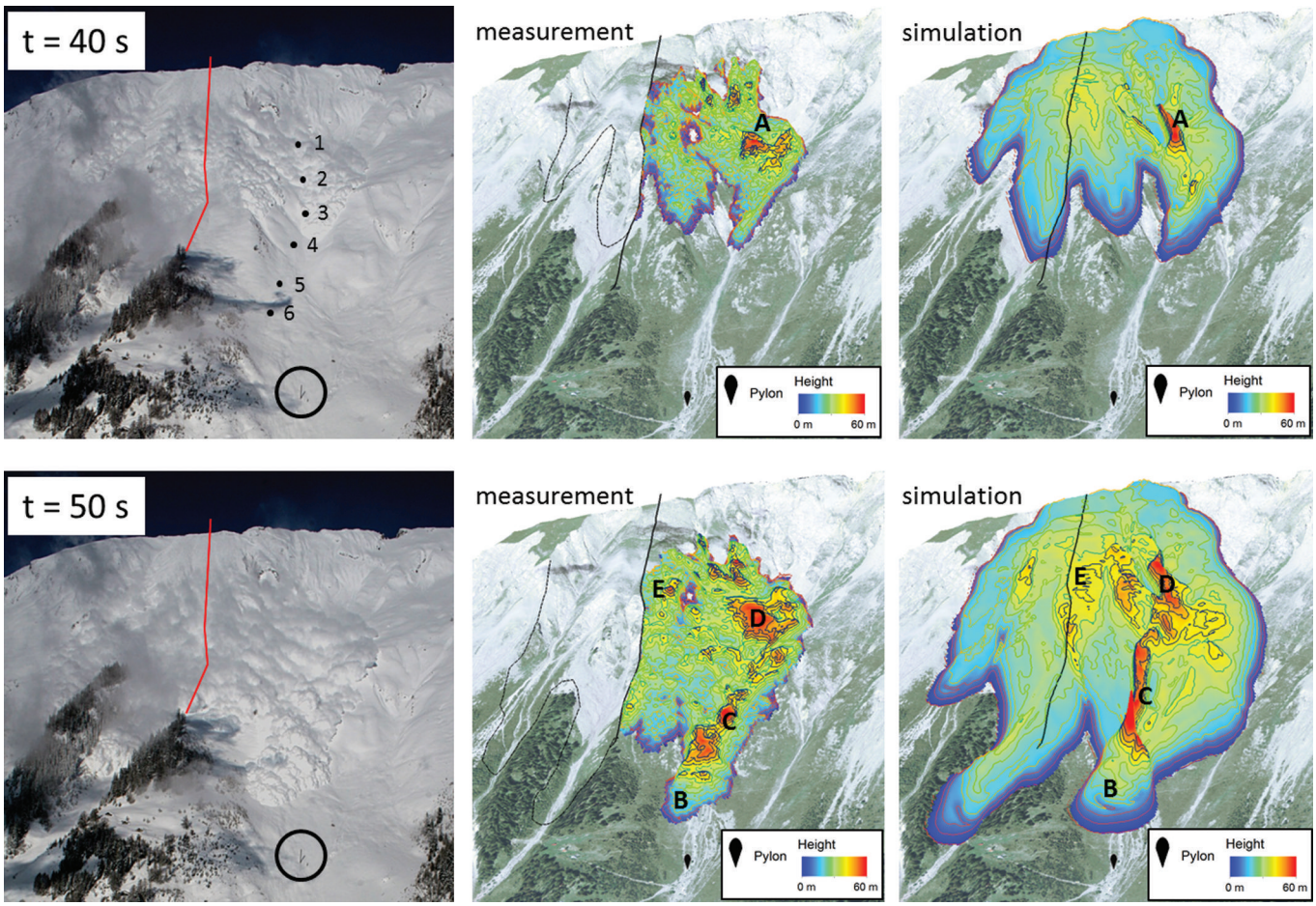

Fig. 9. Powder cloud of avalanche No. 816 at $t = 40$ s (upper row) and $t = 50$ s (lower row) with photogrammetric reconstruction (middle column) and calculated powder-cloud height (right column). The powder-cloud surface on the right-hand side of the cut-off line was reconstructed using photogrammetric methods while the surface on the left-hand side was obscured by clouds (depicted by a black dotted line). The cut-off line is drawn in red in the photographs (left) and black in the maps (middle and right). The pylon is marked by a black circle. Black dots indicate the measurement points 1–6. Letters A–E on the powder cloud surface represent plumes identified in the measurements.

leading to the production of free mechanical energy during entrainment. In the mean, the production coefficient for avalanche No. 816 is the same as for avalanche No. 628 ($\alpha = 0.08$), but in the simulation of the No. 816 avalanche we assumed the production to be higher at the avalanche front (where snow entrainment occurs) and lower at the avalanche tail (where no entrainment occurs). This leads to a slightly different avalanche-core structure and stronger blow-outs at the avalanche front. Because of colder snow-cover temperatures in the runout zone of avalanche No. 816, we reduced the decay coefficient from $\beta = 0.85$ to $\beta = 0.65$.

The avalanche reached a maximum flow velocity of $50\,\mathrm{m\,s^{-1}}$, which could be reproduced by the model calculations. More importantly, the three-arm structure of the avalanche could be reconstructed. Figure 9 shows photographs of avalanche No. 816 and compares the reconstructed and simulated powder-cloud heights at $t = 40$ s and $t = 50$ s after release. The location and shape of the avalanche front are modelled well, indicating that the calculated velocities are of the right order. The two developed arms and the partly visible third arm along the cut-off line at $t = 40$ s are calculated and match the measured values. The powder-cloud width and height of the frontal lobe B at $t = 50$ s are reproduced.

Cleft-and-plume structures of the model calculations were compared to the photogrammetric measurements. The plumes A, D and E resemble the measurements in shape and location. Only plume C seems to be shifted laterally. We cannot exclude that wind during the avalanche event caused a drift of the powder cloud. In the video recording, the clouds visible in Figure 9 move slowly from left to right, indicating a gentle breeze. This wind might explain the right lateral shift of plume C in the measured powder-cloud surface compared to the modelled surface. The surface area covered by the calculated powder cloud equals the measured area. However, the reconstructed powder cloud starts below the release area, which is at the very top of the ridge. The model predicts a cloud in the release area, as air with ice dust is expelled immediately after release.

The evolution of the measured and calculated powder cloud is depicted in Figure 10 for points 1–6. The location of the measurement points is illustrated in Figure 9 at $t = 40$ s. Point 1 is situated above the gully on an open slope whereas points 2–4 are located in the gully. Points 5 and 6 lie in open terrain below the gully. Points 1–3 correspond to points A–C in Figure 4; points 4–6 are shifted to the left compared to points D–F. Powder clouds are higher in the gully (points 2–4 of Fig. 10) than on the open slope above the gully (point 1) and still high in the open terrain below the gully (points 5

https://doi.org/10.3189/2016AoG71A532 Published online by Cambridge University Press

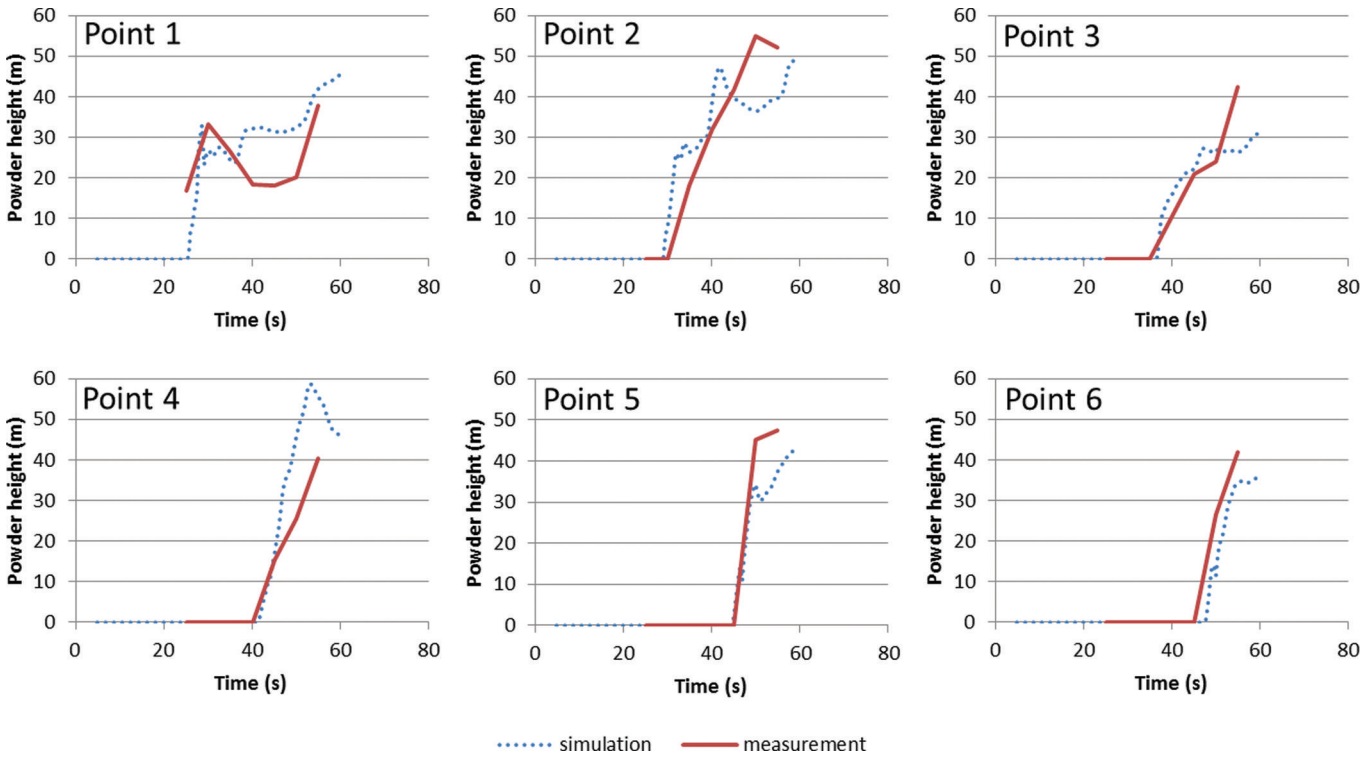

Fig. 10. Height of powder cloud over time at points along the avalanche No. 816 path. Panels are ordered from the topmost point, 1, to the lowest point, 6. The location of the points is marked in Figure 9.

and 6). The calculated powder heights match the measurements well, even though the exact history is not always modelled. For example, at point 1 the calculations model the first peak; however, the deep depression after the peak is not modelled. This indicates that the frontal plume created at this location has moved forward, leaving a depression behind. The rise in time of the powder cloud at points 3–6 is reproduced by the model, suggesting that the blow-out speed coupled with air entrainment is approximately correct. However, the final powder heights are slightly underestimated. At the lower end of the gully (point 4) the powder heights are overestimated by the model.

6. CONCLUSIONS

Photogrammetric measurements were used to generate 3-D surfaces that describe the spatial and temporal movement of powder-snow avalanches. Photogrammetric methods were applied at the Vallée de la Sionne test site because of the high counterslope, which provides the necessary viewing angle to capture both the avalanche front and wake in the transit zone. Comparison between measurements and powder-snow avalanche models has hitherto been restricted to leading-edge velocity and mean powder height at the avalanche front (Fukushima and Parker, 1990; Ancey, 2004; Rastello and Hopfinger, 2004; Turnbull and McElwaine, 2007; Turnbull and others, 2007; Carroll and others, 2013). Our 3-D surface reconstructions from photogrammetric images make it possible to compare not only leading-edge velocity but also the lateral spreading of the avalanche. The Vallée de la Sionne test site is also ideal for this purpose because much of the slope is open and therefore the powder-cloud movement in the lateral direction is not constrained by terrain features. Even though today's state-of-the-art cameras would provide more precise measurements, the resolution of the presented photogrammetric measurements (recorded in the 2003/04 and 2005/06 winters) are sufficient to capture plume blow-outs and lobe–cleft structures on the powder-cloud surface. These can be used to determine the variation in avalanche velocity between the front and wake. Photogrammetric measurements provide an overview description of powder snow motion and, when coupled with isolated point measurements, are a useful method for (1) constraining momentum exchanges between the avalanche core and cloud, (2) identifying powder-cloud drag in both the downslope and lateral flow directions and (3) quantifying air entrainment. The photogrammetric measurements could be further improved by increasing the base distance between the recording cameras. At the Vallée de la Sionne test site the positioning of the cameras is restricted by the topography of the counterslope. A possibility for overcoming these limitations would be to record the avalanche events with, for example, unmanned aerial systems.

The comparison between the photogrammetric measurements and model calculations revealed that many features of the powder cloud could be reproduced by a two-layer model that divided the avalanche into a flowing core and powder cloud. The speed, flow width and mean powder-cloud height were accurately represented, both at the leading edge and wake of the avalanche. Powder height and the formation of blow-out plumes at the front of the avalanche could be modelled by coupling density variations in the avalanche core to air intake and ice-dust blow-out. However, subsequent air entrainment processes smooth the cloud surface and the fine structure of the cloud is lost. The height of the cloud at the avalanche edges appears too great; deep cleft depressions on the cloud surface disappear. Simulating such features will require a model that captures 3-D effects, including the inertia of the blow-out process

https://doi.org/10.3189/2016AoG71A532 Published online by Cambridge University Press

and the formation of turbulent eddies. Such an approach is clearly beyond the scope of the engineering model presented in this paper.

ACKNOWLEDGEMENTS

We thank Florence Naaim and an anonymous reviewer as well as the editor Nicolas Eckert and the chief editor Graham Cogley for helping to improve the quality of the manuscript. We also thank Lucinda Laranjeiro for the 3-D interpretation of the stereo images.

REFERENCES

Ancey C (2004) Powder snow avalanches: approximation as non-Boussinesq clouds with a Richardson number-dependent entrainment function. *J. Geophys. Res.*, **109**, F01005 (doi: 10.1029/2003JF000052)

Bartelt P, Buser O and Platzer K (2006) Fluctuation–dissipation relations for granular snow avalanches. *J. Glaciol.*, **52**(179), 631–643 (doi: 10.3189/172756506781828476)

Bartelt P, Bühler Y, Buser O, Christen M and Meier L (2012) Modeling mass-dependent flow regime transitions to predict the stopping and depositional behavior of snow avalanches. *J. Geophys. Res.*, **117**, F01015 (doi: 10.1029/2010JF001957)

Bartelt P, Bühler Y, Buser O and Ginzler C (2013) Plume formation in powder snow avalanches. In Naaim-Bouvet F, Durand Y and Lambert R eds *International Snow Science Workshop, 7–11 October 2013, Grenoble–Chamonix Mont Blanc. Proceedings*. International Snow Science Workshop, Grenoble, 576–582

Bartelt P, Buser O, Vera Valero C and Bühler Y (2015a) Configurational energy and the formation of mixed flowing/powder snow and ice avalanches. *Ann. Glaciol.*, **57**(71), 179–188 (doi: 10.3189/2016AoG71A464) (see paper in this volume)

Bartelt P, Vera Valero C, Feistl T, Christen M, Bühler Y and Buser O (2015b) Modelling cohesion in snow avalanche flow. *J. Glaciol.*, **61**(229), 837–850 (doi: 10.3189/2015JoG14J126)

Bozhinskiy AN and Losev KS (1998) The fundamentals of avalanche science. Eidg. Inst. Schnee- Lawinenforsch. 55

Buser O and Bartelt P (2009) Production and decay of random kinetic energy in granular snow avalanches. *J. Glaciol.*, **55**(189), 3–12 (10.3189/002214309788608859)

Buser O and Bartelt P (2011) Dispersive pressure and density variations in snow avalanches. *J. Glaciol.*, **57**(205), 857–860 (doi: 10.3189/002214311798043870)

Buser O and Bartelt P (2015) An energy-based method to calculate streamwise density variations in snow avalanches. *J. Glaciol.*, **61**(227), 563–575 (doi: 10.3189/2015JoG14J054)

Carroll CS, Louge MY and Turnbull B (2013) Frontal dynamics of powder snow avalanches. *J. Geophys. Res.*, **118**(2), 913–924 (doi: 10.1002/jgrf.20068)

Christen M, Kowalski J and Bartelt P (2010) RAMMS: numerical simulation of dense snow avalanches in three-dimensional terrain. *Cold Reg. Sci. Technol.*, **63**(1–2), 1–14 (doi: 10.1016/j.coldregions.2010.04.005)

Frauenfelder R and 6 others (2014) Analysis of an artificially triggered avalanche at the Nepheline Syenite Mine on Stjernøya, Alta, Northern Norway. In *A Merging of Theory and Practice: International Snow Science Workshop, 29 September–3 October 2014, Banff, Alberta, Canada. Proceedings*. International Snow Science Workshop, Banff, 689–696

Fukushima Y and Parker G (1990) Numerical simulation of powder-snow avalanches. *J. Glaciol.*, **36**(123), 229–237

Honig J, Bartelt P and Bühler Y (2014) West Twin avalanche helicopter involvement – How safe are our pick-up locations? In *A Merging of Theory and Practice: International Snow Science Workshop, 29 September–3 October 2014, Banff, Alberta, Canada. Proceedings*. International Snow Science Workshop, Banff, 356–363

Nazarov AN (1991) Mathematical modeling of a snow-powder avalanche in the framework of the equations of two-layer shallow water. *Fluid Dyn.*, **26**(1), 70–75 (doi: 10.1007/BF01050115)

Rastello M and Hopfinger EJ (2004) Sediment-entraining suspension clouds: a model of powder-snow avalanches. *J. Fluid Mech.*, **509**, 181–206 (doi: 10.1017/S0022112004009322)

Sovilla B and 11 others (2005) Avalanche dynamics experimental site 'Vallée de la Sionne' Arbaz, Valais – Final report winter 2003/2004, Internal Report Nr. 735. (Technical report) WSL Institute for Snow and Avalanche Research SLF, Davos

Steinkogler W, Sovilla B and Lehning M (2014) Influence of snow cover properties on avalanche dynamics. *Cold Reg. Sci. Technol.*, **97**(0), 121–131 (doi: 10.1016/j.coldregions.2013.10.002)

Turnbull B and McElwaine JN (2007) A comparison of powder-snow avalanches at Vallée de la Sionne, Switzerland, with plume theories. *J. Glaciol.*, **53**(180), 30–40 (doi: 10.3189/172756507781833938)

Turnbull B, McElwaine JN and Ancey C (2007) Kulikovskiy–Sveshnikova–Beghin model of power snow avalanches: development and application. *J. Geophys. Res.*, **112**, F01004 (doi: 10.1029/2006JF000489)

Vallet J, Turnbull B, Joly S and Dufour F (2004) Observations on powder snow avalanches using videogrammetry. *Cold Reg. Sci. Technol.*, **39**(2), 153–159 (doi: 10.1016/j.coldregions.2004.05.004)

Wicki P (2004) Videogrammetrische Auswertung der Lawinenereignisse im Vallée de la Sionne – Winter 2003/04, Internal Report. (Technical report) Swiss Federal Institute for Forest, Snow and Landscape Research WSL, Davos

Wicki P (2005) Photogrammetrie bewegter Objekte mit digitalen Amateur-Kameras. *Geomat. Schweiz*, **9**, 520–522 (doi: 10.5169/seals-236259)

Wicki P and Laranjeiro L (2007) Photogrammetrische Erfassung von Fliess- und Staublawinen mit digitalen Amateur-Kameras. *Geomat. Schweiz*, **6**, 306–309 (doi: 10.5169/seals-236430)